

Article

One-Pot Synthesis of Bismuth Sulfide Nanostructures as an Active Electrode Material for Aqueous Hybrid Capacitors

Adam Moyseowicz  and Agata Moyseowicz *

Department of Process Engineering and Technology of Polymer and Carbon Materials, Faculty of Chemistry, Wrocław University of Science and Technology, Gdańska 7/9, 50–344 Wrocław, Poland; adam.moyseowicz@pwr.edu.pl

* Correspondence: agata.moyseowicz@pwr.edu.pl; Tel.: +48–713206266

Abstract: The high theoretical capacity of Bi_2S_3 shows high promise as a negative electrode material for energy storage devices. Herein, we investigate a facile, one-step chemical precipitation method using common organic solvents, such as acetone, ethanol, and isopropanol, for the synthesis of Bi_2S_3 nanostructures. The nanospherical Bi_2S_3 from acetone ($\text{Bi}_2\text{S}_3\text{-A}$) presents the most balanced electrochemical properties, exhibiting a high specific capacity of 181 mAh g^{-1} at 1 A g^{-1} and decent rate capability. Additionally, $\text{Bi}_2\text{S}_3\text{-A}$ is used as a negative electrode in an aqueous hybrid system with an activated carbon positive electrode, demonstrating a capacitance of 86 F g^{-1} , a specific energy of 7.6 Wh kg^{-1} , and an initial capacity retention of 74% after 1000 cycles.

Keywords: bismuth sulfide; electrode material; energy storage



Citation: Moyseowicz, A.; Moyseowicz, A. One-Pot Synthesis of Bismuth Sulfide Nanostructures as an Active Electrode Material for Aqueous Hybrid Capacitors. *Energies* **2021**, *14*, 2670. <https://doi.org/10.3390/en14092670>

Academic Editor: Teuvo Suntio

Received: 8 April 2021

Accepted: 30 April 2021

Published: 6 May 2021

Publisher's Note: MDPI stays neutral with regard to jurisdictional claims in published maps and institutional affiliations.



Copyright: © 2021 by the authors. Licensee MDPI, Basel, Switzerland. This article is an open access article distributed under the terms and conditions of the Creative Commons Attribution (CC BY) license (<https://creativecommons.org/licenses/by/4.0/>).

1. Introduction

The development of energy storage systems is currently flourishing due to the growing demand for systems that can deliver high amounts of energy. Lithium-ion batteries, electrochemical capacitors, supercapacitors, and their combination as supercapatteries are used in many portable devices, and it is necessary to develop these devices to deliver high power/energy densities in a relatively short period of time. Among the many materials that are used as electrode materials in the discussed devices, the most known are activated carbons (ACs) [1–3]. Other carbon materials, such as carbon nanofibers and nanotubes or graphene and reduced graphene oxide, have been increasingly considered for energy storage devices [4–6]. However, the capacitance of carbon materials is limited by the electric double layer (EDL) due to the specific surface area, which is a crucial factor [7–9]. In addition to carbon materials, materials with pseudocapacitive properties as transition metal oxides/hydroxides have been intensively considered for application in pseudocapacitors due to their fast redox reactions and high specific capacitance. Transition metal oxides and/or hydroxides are characterized by high resistance values, which are undesirable in energy storage devices [10,11]. To manage the current requirements, innovative materials with high specific capacitance and low resistance have been increasingly studied. A novel group of electrode materials are transition metal sulfides, which combine the most important features for being competitive in comparison to carbon materials and metal oxides/hydroxides. Transition metal sulfides are characterized by extremely high specific capacitance values and semiconducting properties. Among various transition metal sulfides, such as CuS , CoS , Ni_2S_3 , MnS , and MoS_2 , Bi_2S_3 seems to be the most attractive material for energy storage and conversion devices [12–17]. The extraordinary features of bismuth sulfide include its unique electric properties resulting from its semiconductor behavior with a direct band gap of 1.3 eV and a high capacitance value; thus, Bi_2S_3 shows tremendous promise. Recently, a large amount of effort has been exerted to explore a new concept of electrochemical capacitors called hybrid capacitors based on electrodes with EDL or pseudocapacitive properties that are combined with

transition metal compounds with battery-like responses [18–20]. Zong et al. [21] combined defect-rich bismuth sulfides with nitrogen-doped carbon nanofibers, and this material exhibited an improved electrochemical performance in a 6 M KOH electrolyte. Another study reported by Liang et al. [22] described an asymmetric hybrid capacitor based on a positive electrode of $\text{NiCo}_2\text{S}_4/\text{Ni}(\text{OH})_2/\text{PPy}$ core-shell structures and a negative electrode of activated carbon, achieving a high energy density of 34.6 Wh kg^{-1} at a power density of 120 W kg^{-1} . Current works indicate that the design and fabrication of hybrid capacitors show promising results; however, the synthesis of battery-like electrode materials using a facile approach remains a very large challenge.

Currently, various morphologies of Bi_2S_3 nanostructures, including nanorods, nanoribbons, hexagonal plates, lamellar platelets, spherical nanoparticles, or their mixtures, can be synthesized in a controlled manner [23]. Notably, the synthesis method can affect the morphology of Bi_2S_3 [24], while the simplicity of Bi_2S_3 synthesis plays an important role from an application point of view. In this paper, we propose using various solvents such as isopropanol, ethanol, acetone, and water for a one-pot synthesis of Bi_2S_3 that can be differentiated by its morphology, crystalline structure, and electrochemical performance. Furthermore, we assemble an aqueous hybrid capacitor with battery-like Bi_2S_3 and EDL AC electrodes and investigate its electrochemical performance, demonstrating the decent specific energy and cycling stability of the device.

2. Materials and Methods

2.1. Materials Synthesis

Bismuth sulfides were chemically precipitated at 75°C [25]. The appropriate amount of bismuth nitrate hexahydrate ($\text{Bi}(\text{NO}_3)_3 \cdot 6\text{H}_2\text{O}$) was dissolved in 200 mL of ethanol, isopropanol, acetone, and distilled water. The solvents were heated to a set temperature of 75°C under mechanical stirring. Subsequently, the aqueous solution of ammonium sulfide ($(\text{NH}_4)_2\text{S}$) was slowly dropped until the dark brown/black colored solution appeared. The as-prepared bismuth sulfides were washed and centrifugated five times. Finally, the resulting materials were dried under vacuum at 60°C for 24 h. The Bi_2S_3 samples were labelled according to the solvent used: ethanol (E), isopropanol (I), acetone (A), and distilled water (W): $\text{Bi}_2\text{S}_3\text{-E}$, $\text{Bi}_2\text{S}_3\text{-I}$, $\text{Bi}_2\text{S}_3\text{-A}$, and $\text{Bi}_2\text{S}_3\text{-W}$, respectively.

2.2. Characterization

Synthesized materials have been characterized by their porous structure by nitrogen gas sorption analysis (Quantachrome), the crystalline structure was determined using X-ray diffraction (XRD, Ultima IV Rigaku) measurements and chemical composition of the samples were analyzed using X-ray photoelectron spectroscopy (XPS, PHI 5000 VersaProbe). The morphologies of the bismuth sulfides were observed via field-emission scanning electron microscope (FESEM, Merlin Zeiss). Detailed information on the materials characterization, including porous structure parameters, XRD, FESEM, and XPS setup and analysis conditions are described in Supplementary Materials.

2.3. Electrochemical Measurements

Electrochemical performance of the electrodes' were determined in a three-electrode setup (SwagelokTM, France) in a 6 M KOH electrolyte using BioLogic VSP potentiostat-galvanostat with an $\text{Hg}|\text{HgO}$ reference electrode and pitch-based activated carbon counter electrode. The electrochemical measurements included cyclic voltammetry (CV) and galvanostatic charge-discharge (GCD) experiments at different current densities and electrochemical impedance spectroscopy (EIS). The detailed procedure for the electrochemical characterization is included in Supplementary Materials.

The specific capacity was expressed in mAh per mass of active material in one electrode. The specific capacity values ($Q_s/\text{mAh g}^{-1}$) were calculated from the cyclic voltammetry curves and galvanostatic discharge profiles using Equations (1) and (2), respectively.

$$Q_s = \frac{\int IdV}{3.6\nu m_{el}} \quad (1)$$

$$Q_s = \frac{I\Delta t}{3.6m_{el}} \quad (2)$$

where I is the current (A), Δt is the discharge time (s), ν is the scan rate (V s^{-1}), and m_{el} is the mass of the active material in the electrode (g).

For the two-electrode Swagelok™ cell, a hybrid device with a Bi_2S_3 negatrod and pitch-based AC positrod ($\text{Bi}_2\text{S}_3\text{-A/AC}$) was assembled at a negative electrode:positive electrode mass ratio of 1:2 (4–5 and 9–10 mg, respectively). The gravimetric cell capacitance (C_{cell}) was calculated using Equation (3) [26]:

$$C_{cell} = \frac{2I \int Vdt}{M \times (V_i^2 - V_f^2)} \quad (3)$$

where I is the discharge current (A), $\int Vdt$ is the integrated area under the galvanostatic discharge curve, M is the total mass of the electrodes (g), and V_i – V_f is the operating discharge voltage from initial to final potential values. Additionally, electrochemical impedance spectroscopy (EIS) measurements in the frequency range of 400 kHz to 10 mHz at an AC amplitude of 5 mV were performed for the assembled device along with cycling stability tests at a current density of 1 A g^{-1} .

The specific energy (E in Wh kg^{-1}) and specific power delivered (P in kW kg^{-1}) by a hybrid capacitor were calculated using Equations (4) and (5), respectively:

$$E = \frac{I \int Vdt}{M \times 3.6} \quad (4)$$

$$P = \frac{3.6 \times E}{t} \quad (5)$$

3. Results and Discussion

The porous structure of the synthesized Bi_2S_3 using various solvents was recognized by N_2 sorption at 77 K. The mesoporous character of all bismuth sulfides are corroborated by the hysteresis loops (Figure 1). The BET surface area of obtained samples was relatively low, as suspected for pristine inorganic materials. The highest BET value of $32 \text{ m}^2 \text{ g}^{-1}$ was noticed for $\text{Bi}_2\text{S}_3\text{-E}$, while the lowest value of $17 \text{ m}^2 \text{ g}^{-1}$ for $\text{Bi}_2\text{S}_3\text{-I}$. The structural parameters of the obtained samples are included in Table 1. Moreover, among the four discussed samples, two groups with comparable porous structure parameters can be distinguished. The first group consists of the Bi_2S_3 samples synthesized using acetone and ethanol as solvents, while the second group consists of bismuth sulfides obtained in isopropanol and water environments. Notably, within both groups, it is clearly seen that the porous texture of Bi_2S_3 is more developed when the synthesis is carried out using acetone and ethanol as solvents. The V_T of the samples ranges from $0.080 \text{ cm}^3 \text{ g}^{-1}$ to $0.121 \text{ cm}^3 \text{ g}^{-1}$ for $\text{Bi}_2\text{S}_3\text{-W}$ and $\text{Bi}_2\text{S}_3\text{-A}$, respectively. Some differences are observed in the case of V_{mes} , which varies from $0.067 \text{ cm}^3 \text{ g}^{-1}$ for $\text{Bi}_2\text{S}_3\text{-I}$ to $0.088 \text{ cm}^3 \text{ g}^{-1}$ for $\text{Bi}_2\text{S}_3\text{-A}$.

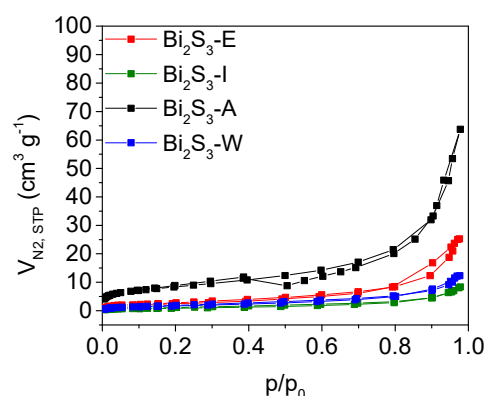


Figure 1. Adsorption/desorption isotherms at 77 K for the bismuth sulfides.

Table 1. Obtained porous structure parameters based on the N₂ isotherms for the bismuth sulfides synthesized with different solvents.

Symbol	S_{BET} $\text{m}^2 \text{g}^{-1}$	V_{T} $\text{cm}^3 \text{g}^{-1}$	V_{mes} $\text{cm}^3 \text{g}^{-1}$	V_{DR} $\text{cm}^3 \text{g}^{-1}$
Bi ₂ S ₃ -A	29	0.121	0.088	0.011
Bi ₂ S ₃ -E	32	0.104	0.085	0.012
Bi ₂ S ₃ -I	17	0.083	0.067	0.006
Bi ₂ S ₃ -W	18	0.080	0.072	0.007

The XRD patterns (Figure 2) present different crystalline structures depending on the synthesis solvent. An amorphous phase is recorded for Bi₂S₃-A and Bi₂S₃-E. The XRD pattern of Bi₂S₃-I reveals the appearance of some characteristic of a primitive orthorhombic crystalline structure of Bi₂S₃ (JCPDS 17-0320). Results can suggest that when isopropanol is applied as the synthesis solvent, crystalline structure is not fully formed and isopropanol led to intermediate form between crystalline and amorphous phase. Moreover, the crystalline phase of Bi₂S₃ is clearly observed when water is the synthesis environment, and the diffraction peaks correlate with the Bi₂S₃ orthorhombic phase. The diffraction planes are assigned in agreement with the standard diffraction pattern of Bi₂S₃ (JCPDS 65-2435). The different crystalline structures of the obtained bismuth sulfides indicate that the kind of solvent strictly affects the crystalline structure. In addition to the influence of the solvent type, the formation of crystalline structure of bismuth sulfide can be also achieved by the Bi₂S₃ treatment at a growing temperature [27]. No impurities or Bi₂O₃ phases are observed in the materials synthesized via the proposed precipitation method with ammonium sulfide.

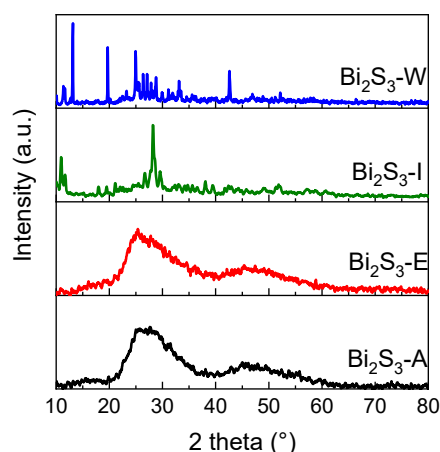


Figure 2. XRD patterns of the synthesized materials.

FESEM was employed to compare and contrast the surface morphologies of the bismuth sulfides synthesized using various solvents. The observations reveal discernible differences in the Bi_2S_3 morphologies (Figure 3). The use of distinct solvents leads to Bi_2S_3 with different particle shapes. Coral-like particles of Bi_2S_3 are obtained when ethanol or acetone is used as the solvent. However, the Bi_2S_3 -E particles are significantly smaller than the Bi_2S_3 -A particles and do not exceed 100 nm, whereas the Bi_2S_3 -A particles can have a diameter of 250 nm. Moreover, the size of particles can affect the porous structure of Bi_2S_3 . It was observed that the size of bismuth sulfide particles increases in the sequence $\text{Bi}_2\text{S}_3\text{-E} < \text{Bi}_2\text{S}_3\text{-A} < \text{Bi}_2\text{S}_3\text{-W} < \text{Bi}_2\text{S}_3\text{-I}$, which is in accordance with the decreasing BET surface area of bismuth sulfides.

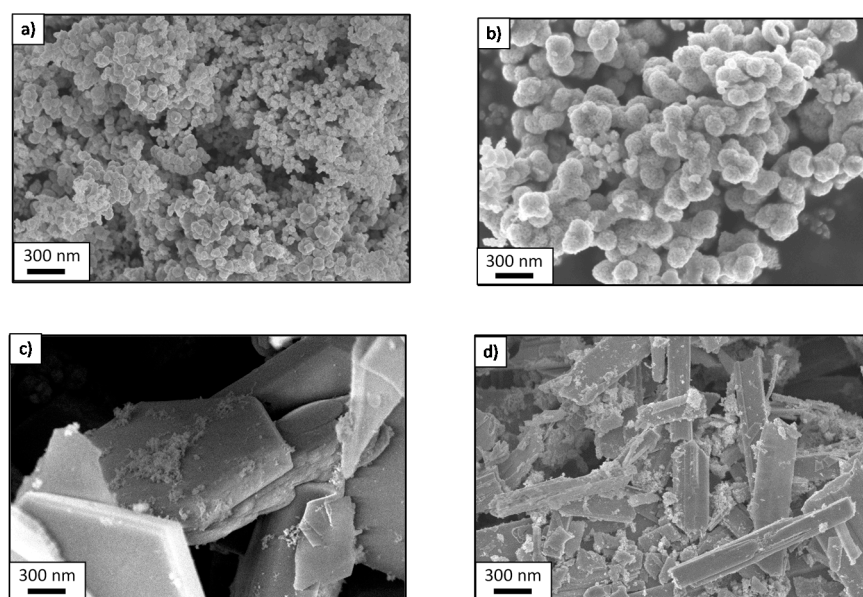


Figure 3. FESEM images of the bismuth sulfides synthesized in ethanol (a), acetone (b), isopropanol (c), and distilled water (d).

To further analyze the surface chemical composition and oxidation state of the Bi_2S_3 samples synthesized in different solvents, XPS was performed, and the results are shown in Figure 4. The XPS survey spectra presented in Figure 4a explicitly reveal the presence of only Bi and S, suggesting the purity of the obtained bismuth sulfides. The Bi and S peak positions agree well with those in other papers [23,24]. The high-resolution Bi 4f and S 2p spectra of the obtained bismuth sulfides are shown in Figure 4b–e. The two strong peaks at binding energies of 158.9 and 164.2 eV correspond to the Bi 4f_{7/2} and Bi 4f_{5/2} in Bi_2S_3 , respectively [28]. The bismuth sulfides synthesized using ethanol, isopropanol, and acetone as solvents are characterized by the nearly symmetrical shape of their peaks, which is attributed to the pure phase of the Bi_2S_3 surface. In the case of bismuth sulfide obtained in water, two extra signals, leading to some distortions on the shoulders of the Bi 4f_{7/2} and Bi 4f_{5/2} peaks, are observed. This feature can be attributed to the heterogeneous composition on the surface of Bi_2S_3 . Moreover, the two peaks with lower intensity located between Bi 4f_{7/2} and Bi 4f_{5/2} can be ascribed to S 2p_{3/2} (161.1 eV) and S 2p_{1/2} (162.2 eV), confirming the valence state of sulfur as S^{2-} [29].

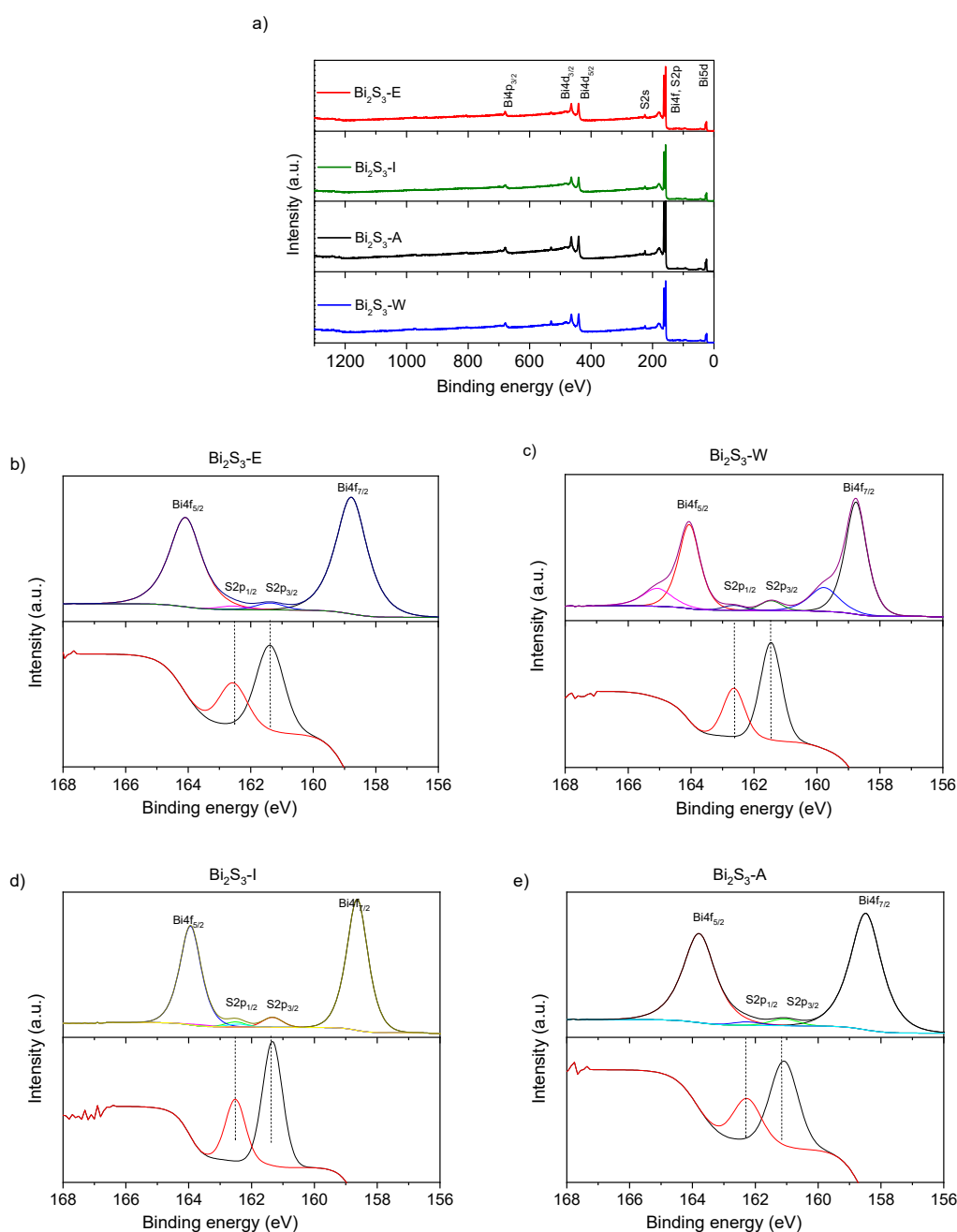


Figure 4. XPS survey spectra (a), Bi 4f and S 2p regions of Bi_2S_3 (upper graph and lower graph, indicated within yellow color range, respectively), regions of Bi_2S_3 obtained in various solvents (b–e).

The results of the CV measurements, presented in Figure 5, show distinguishable redox peaks related to the faradaic reactions of the Bi_2S_3 nanostructures. At a low scan rate, where the current response is diffusion controlled, two pairs of anodic/cathodic peaks appear [30]. The first pair is attributed to the reaction of Bi_2S_3 with OH^- ions, and this pair originates from the change in the bismuth valence state (-0.6 and -0.45 V, Figure 5a) [23]. Moreover, Bi_2S_3 prepared from isopropanol presents a peak shift towards more negative values compared with the rest of the synthesized materials. The second pair is related to the adsorption of hydrogen in the lamellar structure of Bi_2S_3 (-0.85 V), while the anodic peak at -0.3 V is related to hydrogen oxidation during the electrochemical measurements. [25,31] As the scan rate increases to 100 mV s^{-1} (Figure 5b,c), the cathodic peaks become very wide, and a shift of both the anodic and cathodic redox peaks is observed, indicating the

change in the internal resistance of the electrode and the quasi-reversible nature of the faradaic reaction. The faradaic reaction of bismuth sulfide is described according to the following Equation:

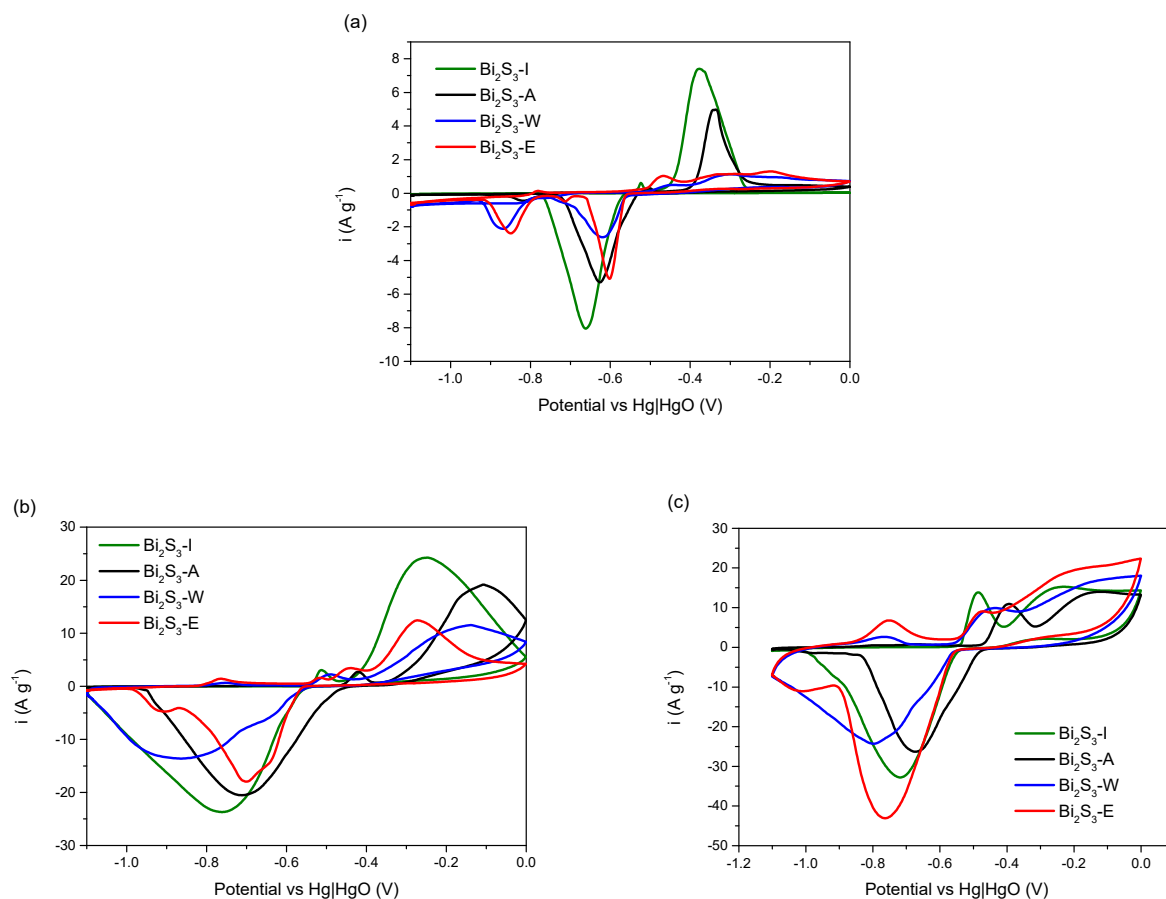
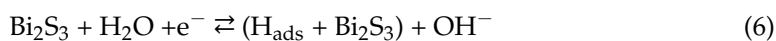


Figure 5. Cyclic voltammograms of the bismuth sulfides synthesized in different solvents at 1, 10, and 100 mV s^{-1} (a–c).

In accordance with the CV results, the GCD discharge curves of the Bi_2S_3 electrodes (Figure 6a) show a distinct plateau at a potential of approximately -0.6 V, indicating the battery-like behavior of the charge storage mechanism. At a current density of 0.5 A g^{-1} , a smaller plateau, which is related to hydrogen adsorption and is observable in the CV measurements at a potential of -0.85 V, does not appear due to diffusion limitations [31]. At a higher current density of 10 A g^{-1} , changes in the charging curve occur in the Bi_2S_3 electrodes as the slope becomes more capacitive in nature. The longest charge–discharge time among all materials at 0.5 A g^{-1} is observed for Bi_2S_3 -I; however, under increasing current regimes, its charge storage capability decreases compared with other materials (Figure 6b). These results indicate that the formed crystalline structure and hexagonal nanoplatelet morphology lead to the highest specific capacity values, but in terms of rate capability, the more amorphous structure and spherical-like particles of Bi_2S_3 -A are more favorable traits. These observations can be related to the degree of crystallinity of the material; for instance, more amorphous/enriched defects in the structure of a material exhibiting Nernstian features allows for the distribution of redox reactions over a wider potential range, thereby translating to improved electrochemical performance at higher scan rates [32].

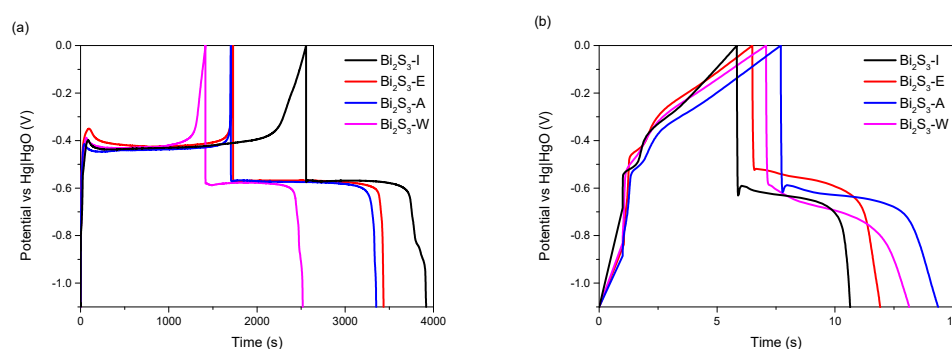


Figure 6. Charge–discharge profiles of the bismuth sulfides recorded at 0.5 A g^{−1} (a) and 10 A g^{−1} (b).

The relationships between the specific capacity and scan rate are presented in Figure 7a, while the specific capacity vs. discharge current density relationship is shown in Figure 7b. The highest specific capacity at a scan rate of 1 mV s^{−1} is achieved by Bi₂S₃-I, with a value of 247 mAh g^{−1}, while the lowest value of 169 mAh g^{−1} is recorded for Bi₂S₃-W. From the galvanostatic charge–discharge measurements, Bi₂S₃-I exhibits a specific capacity of 204 mAh g^{−1} at a current density of 0.5 A g^{−1}, followed by Bi₂S₃-E, Bi₂S₃-A and Bi₂S₃-W, which present specific capacities of 189, 187, and 135 mAh g^{−1}, respectively. The fully crystalline structure of Bi₂S₃-W and its nanorod-like morphology does not provide enough active sites for redox reactions; thus, its charge storage capability is the lowest among all materials. Moreover, bismuth sulfide prepared in acetone and water presents the best rate capability among all samples, maintaining 25 and 29% of the initial capacity at a high current density of 20 A g^{−1}, respectively. Bi₂S₃-I exhibits the highest recorded capacity, while Bi₂S₃-A is a more rational choice for electrochemical applications, as its charge storage properties do not decrease as fast as the material obtained from isopropanol. Among other reported bismuth sulfides, Bi₂S₃ synthesized from organic solvents such as acetone, isopropanol, and ethanol exhibits higher specific capacities due to its stable electrochemical performance over a wide working potential window (Table 2).

Table 2. Comparison of the electrochemical properties of the Bi₂S₃-based materials synthesized under different conditions.

Sample Name	Synthesis Method	Morphology	Electrolyte	Specific Capacity *	Cycling Stability	Ref.
Bi ₂ S ₃	Self-sacrificial template method	Nanorod-stacked hollow microtubes	1 M KOH	148 mAh g ^{−1} at 1 A g ^{−1}	91% after 3000 cycles	[18]
dr-Bi ₂ S ₃ /S-NCNF **	Hydrothermal method	Nanofibers	6 M KOH	175 mAh g ^{−1} at 1 A g ^{−1}	81% after 1000 cycles	[21]
Bi ₂ S ₃ -75 °C	Chemical precipitation	Nanorods	6 M KOH	68 mAh g ^{−1} at 1 A g ^{−1}	52% after 1000 cycles	[25]
Bi ₂ S ₃	Hydrothermal method	Nanoflowers	6 M KOH	40 mAh g ^{−1} at 1 A g ^{−1}	-	[33]
Bi ₂ S ₃	Solvothermal method	Nanorods	1 M Na ₂ SO ₄	53 mAh g ^{−1} at 1 A g ^{−1}	-	[34]
Bi ₂ S ₃ -A	Chemical precipitation	Coral-like nanospheres	6 M KOH	181 mAh g ^{−1} at 1 A g ^{−1}	74% after 1000 cycles	This work
Bi ₂ S ₃ -I	Chemical precipitation	Hexagonal nanoplatelets	6 M KOH	193 mAh g ^{−1} at 1 A g ^{−1}	-	This work

* Specific capacity was calculated according to the respective capacitance and operating voltage of given materials. ** dr-Bi₂S₃/S-NCNF—defect-rich bismuth sulfide/nitrogen-doped carbon nanofibers.

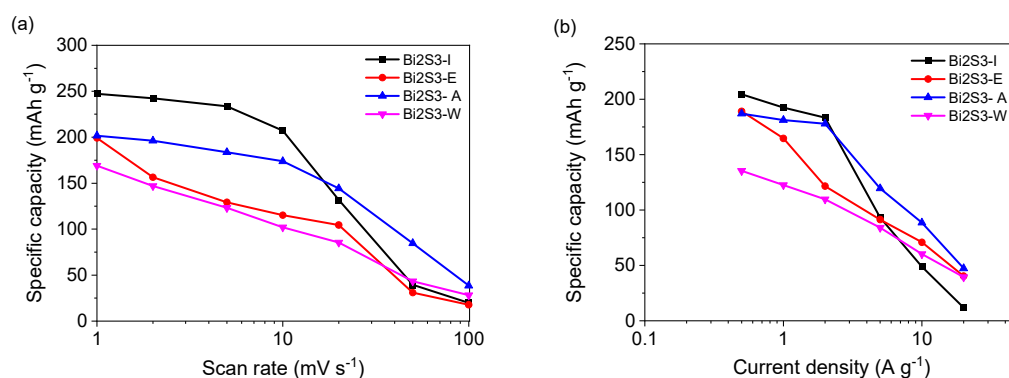


Figure 7. Specific capacity versus scan rate (a) and discharge current density (b) of the bismuth sulfides.

For further evaluation of the application potential of bismuth sulfides, the material with the most balanced specific capacity and rate capability was selected ($\text{Bi}_2\text{S}_3\text{-A}$) as a negatrod for an asymmetric device with an activated carbon positrod. The assembled hybrid capacitor with a battery-type oxidation–reduction reaction and AC with an electrochemical double layer mechanism was investigated in an aqueous 6 M KOH electrolyte. As shown in Figure 8a, the CV curves present an irregular shape with visible peaks, which can be attributed to the combination of the faradaic and non-faradaic capacitance from the transition metal sulfide and carbon electrodes. The quasi-triangular shape of the GCD profile further confirms the capacitive nature of the hybrid capacitor (Figure 8b), indicating its reversible charge–discharge capability [35]. Furthermore, both the negatrod and positrod potential ranges are balanced while the cell is operating, with a clear distinction between the EDL-type GCD curve of the carbon electrode and the battery-like plot of $\text{Bi}_2\text{S}_3\text{-A}$. The assembled hybrid capacitor exhibits a specific capacitance of 104 F g^{-1} at scan rates of 1 mV s^{-1} and 86 F g^{-1} and a current density of 0.2 A g^{-1} , as calculated from the CV and GCD measurements, respectively (Figure 8c). The rate capability at higher scan rates and current regimes is approximately 20–33% due to diffusion-controlled processes at the negatrod [18].

The EIS measurement results of the hybrid capacitor are presented in the form of Nyquist plots, Figure 8d. The small semicircle in the high-frequency region is attributed to the charge transfer resistance (R_{ct}), which is related to the faradaic reactions of Bi_2S_3 [23]. The R_{ct} value of the $\text{Bi}_2\text{S}_3/\text{AC}$ capacitor is 0.25Ω , implying fast charge kinetics. In the low-frequency region, the more inclined the plot is towards the $-Z''$ axis, the lower the resistance attributed to the diffusion of ions at the electrode/electrolyte interface, which for the hybrid device shows certain distortions in the ion movement at both the electrode/electrolyte interfaces; thus, this resistance may explain the capacitive performance drop at higher current densities [36]. The investigated asymmetric system presents an equivalent circuit of the solution resistance and two parallel ladders, one for each electrode [37] (Figure 8d). The fitting of the impedance spectrum presents components such as charge transfer resistance, Warburg impedance related with diffusion of ions and constant phase element (CPE) attributed to the double layer capacitance at the electrodes interface and faradaic reactions of bismuth sulfide [38]. The long-term performance of the hybrid capacitor is an important factor in the evaluation of its applicability for energy storage devices (Figure 9a). The initial drop of 35% is related to the formation of a surface passivation layer and the side reactions related to bismuth sulfide [38]; however, after the 125th cycle, the assembled $\text{Bi}_2\text{S}_3\text{-A}/\text{AC}$ capacitor shows greatly improved stability, retaining 74% of the initial capacitance after 1000 charge–discharge cycles.

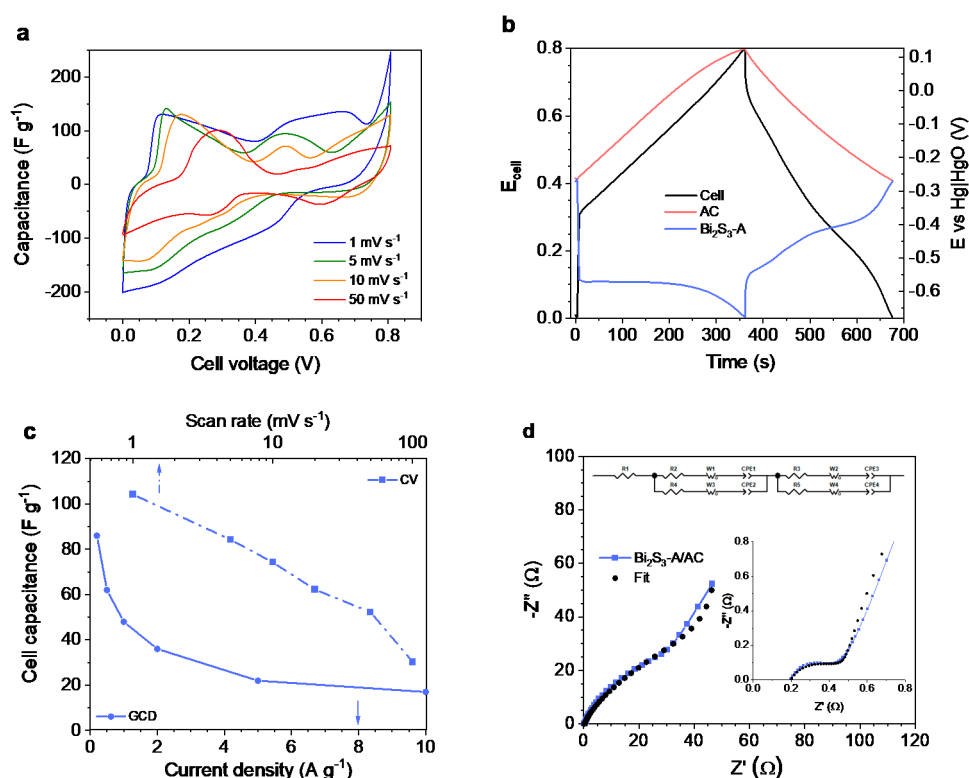


Figure 8. CV curves at the different scan rates (a), GCD curves at a current density of 0.2 A g⁻¹ (b), cell capacitance versus scan rate/discharge current density (c), and the Nyquist plot with an inset representing the high-frequency range and the equivalent circuit diagram (d) of the hybrid capacitor based on the Bi₂S₃-A and AC electrodes.

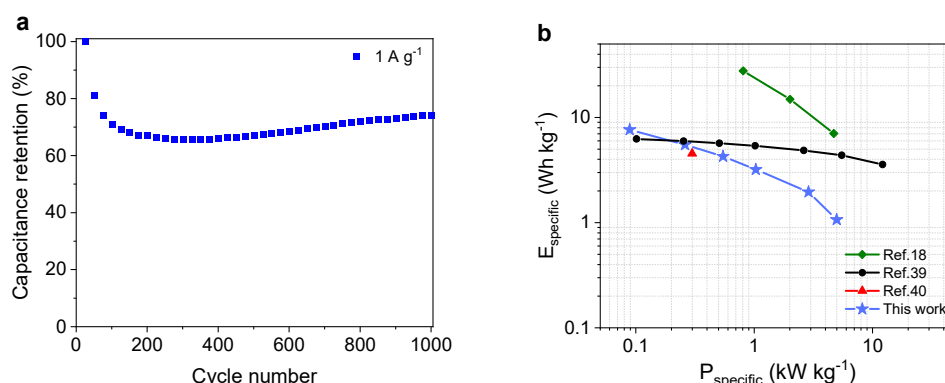


Figure 9. Cycling stability at a current density of 1 A g⁻¹ (a) and the Ragone plot of the specific energy–power density relationship of the hybrid capacitor and other various hybrid devices (b).

The energy storage capability of the Bi₂S₃-A/AC hybrid capacitor was evaluated in the form of a Ragone plot (Figure 9b). The assembled device can reach a maximum specific energy density of 7.6 Wh kg⁻¹ at a specific power density of 0.09 kW kg⁻¹, which is in the medium range/slightly improved compared with the previously reported polyaniline-copypyrrole/thermally reduced graphene oxide composite capacitor [39], Bi₂S₃/CoNi-LDH hybrid capacitor or polyimidazole/CuS/CNT composite [40], and on pair with commercially available devices [41]. However, due to the decreasing capacitive performance at higher current densities, the Bi₂S₃-A/AC hybrid capacitor shows approximately 1 Wh kg⁻¹ of specific energy at a high power density of 5 kW kg⁻¹.

4. Conclusions

In summary, we showed that the one-pot synthesis of bismuth sulfide nanostructures is a promising and economical approach for preparing negative electrodes for hybrid aqueous capacitors. The amorphous coral-like structure of Bi_2S_3 synthesized from an acetone solution provided active sites for faradaic reactions at the electrode/electrolyte interface, yielding high capacity values and reasonable rate capability. Moreover, a hybrid aqueous capacitor assembled with Bi_2S_3 as a negatrod and activated carbon as a positrod exhibited a specific energy density of 7.6 Wh kg^{-1} at a power density of 0.9 W kg^{-1} . The current work provides directions for the successful design of Bi_2S_3 nanostructures to explore the use of high-performance anode materials in potential energy-related applications such as hybrid supercapacitors or aqueous lithium or sodium batteries.

Supplementary Materials: Supplementary materials can be found at <https://www.mdpi.com/article/10.3390/en14092670/s1>.

Author Contributions: Conceptualization, A.M. (Agata Moyseowicz) and A.M. (Adam Moyseowicz); methodology, A.M. (Agata Moyseowicz) and A.M. (Adam Moyseowicz); formal analysis, A.M. (Agata Moyseowicz); investigation, A.M. (Agata Moyseowicz) and A.M. (Adam Moyseowicz); resources, A.M. (Agata Moyseowicz); writing—original draft preparation, A.M. (Agata Moyseowicz) and A.M. (Adam Moyseowicz); writing—review and editing, A.M. (Agata Moyseowicz); visualization, A.M. (Agata Moyseowicz) and A.M. (Adam Moyseowicz); supervision, A.M. (Agata Moyseowicz); funding acquisition, A.M. (Agata Moyseowicz). All authors have read and agreed to the published version of the manuscript.

Funding: The research leading to the above results has received funding from the National Science Centre (Poland) under the grant agreement 2016/21/D/ST5/01642.

Institutional Review Board Statement: Not applicable.

Informed Consent Statement: Not applicable.

Data Availability Statement: No new data were created or analyzed in this study. Data sharing is not applicable to this article.

Conflicts of Interest: The authors declare no conflict of interest. The funders had no role in the design of the study; in the collection, analyses, or interpretation of data; in the writing of the manuscript; or in the decision to publish the results.

References

- Conway, B.E. *Electrochemical Supercapacitors: Scientific Fundamentals and Technological Applications*; Springer: New York, NY, USA, 1999.
- Pandolfo, A.G.; Hollenkamp, A.F. Carbon properties and their role in supercapacitors. *J. Power Sources* **2006**, *157*, 11–27. [\[CrossRef\]](#)
- Kierzek, K.; Frackowiak, E.; Lota, G.; Gryglewicz, G.; Machnikowski, J. Electrochemical capacitors based on highly porous carbons prepared by KOH activation. *Electrochim. Acta* **2004**, *49*, 515–523. [\[CrossRef\]](#)
- Ko, T.-H.; Hung, K.-H.; Tzeng, S.-S.; Shen, J.-W.; Hung, C.-H. Carbon nanofibers grown on activated carbon fiber fabrics as electrode of supercapacitors. *Phys. Scr.* **2007**, *129*, 80–84. [\[CrossRef\]](#)
- Śliwak, A.; Grzyb, B.; Ćwikła, J.; Gryglewicz, G. Influence of wet oxidation of herringbone carbon nanofibers on the pseudocapacitance effect. *Carbon* **2013**, *64*, 324–333. [\[CrossRef\]](#)
- Grzyb, B.; Gryglewicz, S.; Śliwak, A.; Diez, N.; Machnikowski, J.; Gryglewicz, G. Guanidine, amitrole and imidazole as nitrogen dopants for the synthesis of N-graphenes. *RSC Adv.* **2016**, *6*, 15782. [\[CrossRef\]](#)
- Śliwak, A.; Diez, N.; Miniach, E.; Gryglewicz, G. Nitrogen-containing chitosan-based carbon as an electrode material for high-performance supercapacitors. *J. Appl. Electrochem.* **2016**, *46*, 667–677. [\[CrossRef\]](#)
- Raymundo-Pinero, E.; Kierzek, K.; Machnikowski, J.; Beguin, F. Relationship between the nanoporous texture of activated carbons and their capacitance properties in different electrolytes. *Carbon* **2006**, *44*, 2498–2507. [\[CrossRef\]](#)
- Mirzaein, M.; Abbas, Q.; Hunt, M.R.C.; Hall, P. Pseudocapacitive effect of carbons doped with different functional groups as electrode materials for electrochemical capacitors. *Energies* **2020**, *13*, 5577. [\[CrossRef\]](#)
- Brousse, T.; Taberna, P.L.; Crosnier, O.; Dugas, R.; Guillement, P.; Scudeller, Y.; Zhou, Y.; Favier, F.; Bélanger, D.; Simon, P. Long-term cycling behavior of asymmetric activated carbon/ MnO_2 aqueous electrochemical supercapacitor. *J. Power Sources* **2007**, *173*, 633–641. [\[CrossRef\]](#)
- Śliwak, A.; Gryglewicz, G. High-voltage asymmetric supercapacitors based on carbon and manganese oxide/oxidized carbon nanofiber composite electrodes. *Energy Technol.* **2014**, *2*, 819. [\[CrossRef\]](#)

12. Zhang, Z.; Huang, Z.; Ren, L.; Shen, Y.; Qi, X.; Zhong, J. One-pot synthesis of hierarchically nanostructured Ni_3S_2 dendrites as active materials for supercapacitors. *Electrochim. Acta* **2014**, *149*, 316–323. [\[CrossRef\]](#)
13. Wei, W.; Mi, L.; Gao, Y.; Zheng, Z.; Chen, W.; Guan, X. Partial ion-exchange of nickel-sulfide-derived electrodes for high performance supercapacitors. *Chem. Mater.* **2014**, *26*, 3418–3426. [\[CrossRef\]](#)
14. Huang, K.-J.; Zhang, J.Z.; Shi, G.W.; Liu, Y.-M. One-step hydrothermal synthesis of two-dimensional cobalt sulfide for high-performance supercapacitors. *Mater. Lett.* **2014**, *131*, 45–48. [\[CrossRef\]](#)
15. Tie, J.; Han, J.; Diao, G.; Liu, J.; Xie, Z.; Cheng, G.; Sun, M.; Yu, L. Controllable synthesis of hierarchical nickel cobalt sulfide with enhanced electrochemical activity. *Appl. Surf. Sci.* **2018**, *435*, 187–194. [\[CrossRef\]](#)
16. Yang, H.; Xie, J.; Li, C.M. Bi_2S_3 nanorods modified with $\text{Co}(\text{OH})_2$ ultrathin nanosheets to significantly improve its pseudocapacitance for high specific capacitance. *RSC Adv.* **2014**, *4*, 48666–48670. [\[CrossRef\]](#)
17. Durga, I.K.; Rao, S.S.; Reddy, A.E.; Gopi, C.V.V.M.; Kim, H.-J. Achieving copper sulfide leaf like nanostructure electrode for high performance supercapacitor and quantum-dot sensitized solar cells. *Appl. Surf. Sci.* **2018**, *435*, 666–675. [\[CrossRef\]](#)
18. Yu, X.; Zhou, J.; Li, Q.; Zhao, W.-N.; Zhao, S.; Chen, H.; Tao, K.; Han, L. Bi_2S_3 nanorod-stacked hollow microtubes self-assembled from bismuth-based metal–organic frameworks as advanced negative electrodes for hybrid supercapacitors. *Dalton Trans.* **2019**, *48*, 9057–9061. [\[CrossRef\]](#) [\[PubMed\]](#)
19. Ock, I.W.; Choi, J.Q.; Jeong, H.M.; Kang, J.K. Synthesis of pseudocapacitive polymer chain anode and subnanoscale metal oxide cathode for aqueous hybrid capacitors enabling high energy and power densities along with long cycle life. *Adv. Energy Mater.* **2018**, *8*, 1702895. [\[CrossRef\]](#)
20. Ding, J.; Hu, W.; Paek, W.; Mitlin, D. Review of hybrid ion capacitors: From aqueous to lithium to sodium. *Chem. Rev.* **2018**, *118*, 6457–6498. [\[CrossRef\]](#) [\[PubMed\]](#)
21. Zong, W.; Lai, F.; He, G.; Feng, J.; Wang, W.; Lian, R.; Miao, Y.-E.; Wang, G.-C.; Parkin, I.P.; Liu, T. Sulfur-deficient bismuth sulfide/nitrogen-doped carbon nanofibers as advanced free-standing electrode for asymmetric supercapacitors. *Small* **2018**, *14*, 1801562. [\[CrossRef\]](#) [\[PubMed\]](#)
22. Liang, M.; Zhao, M.; Wang, H.; Shen, J.; Song, X. Enhanced cycling stability of hierarchical $\text{NiCo}_2\text{S}_4@\text{Ni}(\text{OH})_2@\text{PPy}$ core–shell nanotube arrays for aqueous asymmetric supercapacitors. *J. Mater. Chem. A* **2018**, *6*, 2482–2493. [\[CrossRef\]](#)
23. Moyseowicz, A.; Moyseowicz, A. Tailoring the morphology, crystalline structure, and electrochemical properties of nanostructured Bi_2S_3 using various solvent mixtures. *Mater. Renew. Sustain. Energy* **2020**, *9*, 11. [\[CrossRef\]](#)
24. Miniach, E.; Gryglewicz, G. Solvent-controlled morphology of bismuth sulfide for supercapacitor applications. *J. Mater. Sci.* **2018**, *53*, 16511–16523. [\[CrossRef\]](#)
25. Moyseowicz, A. Scalable one-pot synthesis of bismuth sulfide nanorods as an electrode active material for energy storage applications. *J. Solid State Electrochem.* **2019**, *23*, 1191–1199. [\[CrossRef\]](#)
26. Laheäär, A.; Przygocki, P.; Abbas, Q.; Béguin, F. Appropriate methods for evaluating the efficiency and capacitive behavior of different types of supercapacitors. *Electrochem. Commun.* **2015**, *60*, 21–25. [\[CrossRef\]](#)
27. Lu, J.; Wang, Z.; Zhang, Y.; Zhou, X. Hydrothermal synthesis of Bi_2S_3 nanorods from a single-source precursor and their promotional effect on the photocatalysis of TiO_2 . *J. Nanomater.* **2013**, 125409. [\[CrossRef\]](#)
28. Li, W.H. Synthesis and characterization of bismuth sulfide nanowires through microwave solvothermal technique. *Mater. Lett.* **2008**, *62*, 243–245. [\[CrossRef\]](#)
29. Lou, W.; Chen, M.; Wang, X.; Liu, W. Novel single-source precursors approach to prepare highly uniform Bi_2S_3 and Sb_2S_3 nanorods via a solvothermal treatment. *Chem. Mater.* **2007**, *19*, 872–878. [\[CrossRef\]](#)
30. Wang, B.; Aoki, K.J.; Chen, J.; Nishiumi, T. Slow scan voltammetry for diffusion-controlled currents in sodium alginate solutions. *J. Electroanal. Chem.* **2013**, *70*, 60–64. [\[CrossRef\]](#)
31. Zhang, B.; Ye, X.; Hou, W.; Zhao, Y.; Xie, Y. Biomolecule-assisted synthesis and electrochemical hydrogen storage of Bi_2S_3 flowerlike patterns with well-aligned nanorods. *J. Phys. Chem. B* **2006**, *110*, 8978–8985. [\[CrossRef\]](#)
32. Eftekhari, A.; Mohamedi, M. Tailoring pseudocapacitive materials from a mechanistic perspective. *Mater. Today Energy* **2017**, *6*, 211–229. [\[CrossRef\]](#)
33. Yue, H.; Chen, S.; Li, P.; Zhu, C.; Yang, X.; Li, T.; Gao, Y. Lemongrass-like Bi_2S_3 as a high-performance anode material for lithium-ion batteries. *Ionics* **2019**, *25*, 3587–3592. [\[CrossRef\]](#)
34. Duca, M.; Guerrini, E.; Colombo, A.; Trasatti, S. Activation of nickel for hydrogen evolution by spontaneous deposition of iridium. *Electrocatal* **2013**, *4*, 338–345. [\[CrossRef\]](#)
35. Zhai, X.; Gao, J.; Xu, X.; Hong, W.; Wang, H.; Wu, F.; Liu, Y. 3D interconnected Bi_2S_3 nanosheets network directly grown on nickel foam as advanced performance binder-free electrode for hybrid asymmetric supercapacitor. *J. Power Sources* **2018**, *396*, 648–658. [\[CrossRef\]](#)
36. Ramasamy, K.; Gupta, R.K.; Sims, H.; Palchoudhury, S.; Ivanov, S.; Gupta, A. Layered ternary sulfide CuSbS_2 nanoplates for flexible solid-state supercapacitors. *J. Mater. Chem. A* **2015**, *3*, 13263–13274. [\[CrossRef\]](#)
37. Fletcher, S.; Black, V.J.; Kirkpatrick, I. A universal equivalent circuit for carbon-based supercapacitors. *J. Solid State Electrochem.* **2014**, *18*, 1377–1387. [\[CrossRef\]](#)
38. Chai, W.; Yin, W.; Wang, K.; Ye, W.; Li, X.; Tang, B.; Rui, Y. Bismuth sulfide–integrated carbon derived from organic ligands as a superior anode for sodium storage. *Energy Technol.* **2019**, *7*, 1900668. [\[CrossRef\]](#)

-
39. Moyseowicz, A.; González, Z.; Menéndez, R.; Gryglewicz, G. Three-dimensional poly(aniline-co-pyrrole)/thermally reduced graphene oxide composite as a binder-free electrode for high-performance supercapacitors. *Compos. B Eng.* **2018**, *145*, 232–239. [[CrossRef](#)]
 40. Ravi, S.; Gopi, C.V.V.M.; Kim, H.J. Enhanced electrochemical capacitance of polyimidazole coated covellite CuS dispersed CNT composite materials for application in supercapacitors. *Dalton Trans.* **2016**, *45*, 12362–12371. [[CrossRef](#)]
 41. Yassine, M.; Fabris, D. Performance of commercially available supercapacitors. *Energies* **2017**, *10*, 1340. [[CrossRef](#)]